

Electrochemical interface between an ionic liquid and a model metallic electrode

Stewart K. Reed, Oliver J. Lanning, and Paul A. Madden

Citation: *J. Chem. Phys.* **126**, 084704 (2007); doi: 10.1063/1.2464084

View online: <http://dx.doi.org/10.1063/1.2464084>

View Table of Contents: <http://jcp.aip.org/resource/1/JCPSA6/v126/i8>

Published by the AIP Publishing LLC.

Additional information on J. Chem. Phys.

Journal Homepage: <http://jcp.aip.org/>

Journal Information: http://jcp.aip.org/about/about_the_journal

Top downloads: http://jcp.aip.org/features/most_downloaded

Information for Authors: <http://jcp.aip.org/authors>



Goodfellow

metals • ceramics • polymers
composites • compounds • glasses

Save 5% • Buy online
70,000 products • Fast shipping

www.goodfellowusa.com

Electrochemical interface between an ionic liquid and a model metallic electrode

Stewart K. Reed, Oliver J. Lanning, and Paul A. Madden

School of Chemistry, University of Edinburgh, Edinburgh EH9 3JJ, Scotland

(Received 6 November 2006; accepted 9 January 2007; published online 26 February 2007)

A molecular dynamics simulation model for an electroactive interface in which a metallic electrode is maintained at a preset electrical potential is described. The model, based on earlier work of Siepmann and Sprik [*J. Chem. Phys.* **102**, 511 (1995)], uses variable charges whose magnitudes are adjusted on-the-fly according to a variational procedure to maintain the constant potential condition. As such, the model also allows for the polarization of the electrode by the electrolyte, sometimes described by the introduction of image charges. The model has been implemented in a description of an electrochemical cell as a pair of parallel planar electrodes separated by the electrolyte using a two-dimensional Ewald summation method. The method has been applied to examine the interfacial structure in two ionic liquids, consisting of binary mixtures of molten salts, chosen to exemplify the influences of dissimilar cation size and charge. The stronger coordination of the smaller and more highly charged cations by the anions prevents them from approaching even the negatively charged electrode closely. This has consequences for the capacitance of the electrode and will also have an impact on the rates of electron transfer processes. The calculated capacitances exhibit qualitatively the same dependence on the applied potential as has been observed in experimental studies. © 2007 American Institute of Physics.

[DOI: [10.1063/1.2464084](https://doi.org/10.1063/1.2464084)]

I. INTRODUCTION

The study of structure and dynamics at an electrochemical interface with realistic models for the interactions presents a substantial challenge for computer simulation. Such calculations should, in principle, allow insights into the factors which control electrode kinetics which are difficult to obtain from direct experiment, such as preferential absorption of ions, the profile of the electrical potential across the interface, the rate of diffusion in the interfacial region, etc. There have been a number of attempts with direct *ab initio* simulation methods, especially for aqueous ionic solutions. Such methods allow for an explicit treatment of the adiabatic electronic structures of the electrode and the electrolyte and their effects on the ion dynamics. However, while giving new insights into the electronic structure at the interface *per se*,^{1,2} these methods have not allowed runs of sufficient length or size to make contact with classical descriptions of electrochemical phenomena. There have also been many classical simulation studies in which the properties of the electrolyte in the vicinity of a wall with a fixed charge density (either smooth or atomically structured) have been examined^{3,4} on longer time and length scales. In some cases, the treatment of the wall has allowed for its polarization by the charges within the electrolyte using an image charge method.⁵ However, even these calculations have some limitations in the representation of the electrolyte interaction with a real metallic electrode. First, real electrodes are held at constant *potential*, rather than constant *charge*. A way to achieve this in an *ab initio* calculation has been given by Lozovoi *et al.*⁵ but has not been applied to bulk simulations. Secondly, as graphically illustrated by the *ab initio* simulations¹

of Halley *et al.*, the electrical potential drop across the interface is strongly affected by screening by the outermost regions of the metallic surface, an effect which is difficult to recapture with a model of classical charges and image charges whose introduction depends on the arbitrary assignment of a surface image plane. The importance of including the image interactions in a description of the electrode/electrolyte interaction has been illustrated in a recent paper.⁶

In this paper we make use of a representation of a metallic electrode within a classical simulation which deals directly with the first of these issues. With an appropriate description of the long-range Coulombic interaction between all charges, we demonstrate quantitative consistency between the behavior of the electrical potential and the induced charges in the simulations and the predictions of classical electrostatic theory. The method also partially addresses the second issue mentioned in the previous paragraph, of the polarization of the electrode by the electrolyte, and avoids the introduction of an arbitrary image plane, though without substantial refinement it cannot provide a realistic description of the screening of the electric field very close to the electrode surface by the outer regions of the metallic charge density. As we will show in a subsequent paper, the ability to control the electrode potential will allow us to calculate directly the rates of electron transfer processes between the electrode and oxidizable and reducible species in the electrolyte. A major advantage of the direct representation of the electrode as a polarizable metal held at constant potential over a constant charge plus image charge model is that it can be applied to nonplanar electrode geometries, which we will exploit in future work.

We describe an application of the model to study the interfacial structure and the interfacial potential at a metal/ionic liquid interface at constant potential. This interface is of enormous technological importance⁷ and, with the advent of low-temperature ionic liquids, it has become possible to carry out detailed experiments on the interfacial structure in Coulomb liquids⁸ (albeit ones in which the electrolyte ions have internal molecular structures, nonspherical shapes, etc.). Previous classical fixed-surface charge simulations^{9–11} (as well as integral equation theories¹²) have indicated that the interfacial ion density and the profile of the interfacial potential depart *qualitatively* from the double layer ideas applied in solution electrochemistry. These findings should be factored into theories of measurements of electrode capacitances, electrode kinetics, etc., which are normally interpreted using double layer ideas, but this does not yet appear to have happened. The improved description of the metallic electrode which we present here should allow a closer connection between the results emerging from simulation and experiment.

II. THE MODEL METALLIC ELECTRODE

The model for the metallic electrodes is derived from the work of Siepmann and Sprik,¹³ who studied the absorption of water molecules at a metal surface and on the tip of a model scanning tunneling microscope probe. An alternative computational scheme with similar properties was introduced by Finnis *et al.*¹⁴ Our electrode consists of several layers of atoms arranged with crystalline order; each atom j carries a Gaussian charge distribution $\rho_j(r)$ which has an integrated charge of q_j and is of fixed width η :

$$\rho_j(\mathbf{r}) = q_j A \exp(-|\mathbf{r} - \mathbf{r}_j|^2 \eta^2), \quad (1)$$

where $A = \eta^3 \pi^{3/2}$ is the normalization constant. The full system consists of two electrodes and a set of melt ions. Each ion in the melt has a point charge, so that its charge distribution is

$$\rho_i(\mathbf{r}) = q_i \delta(\mathbf{r} - \mathbf{r}_i), \quad (2)$$

where $\delta(\mathbf{r} - \mathbf{r}_i)$ is the Kronecker delta function. The total Coulomb energy of this system is

$$U_c = \frac{1}{2} \int \int \frac{\rho(\mathbf{r}') \rho(\mathbf{r}'') d\mathbf{r}' d\mathbf{r}''}{|\mathbf{r}' - \mathbf{r}''|}, \quad (3)$$

where $\rho(\mathbf{r})$ is the total charge density (electrode atoms and melt ions). Note that this expression will contain a self-energy for the interaction of each Gaussian charge density with itself (any self-energy of the point charges is a trivial constant). The potential experienced by any charge is obtained from the partial derivative of this expression with respect to that charge

$$V_j = \left[\frac{\partial U_c}{\partial q_j} \right]_{\{q_i, i \neq j\}}. \quad (4)$$

In Siepmann and Sprik's model for a metal,¹³ the value of the charge on each electrode atom at each time step in a molecular dynamics (MD) procedure is obtained by requiring that

the potential experienced by each charge j in that electrode is a constant V_j^0 , which is the value of the preset electrode potential and will take the same value for all ions in a particular electrode. The potential within the electrode is thus a constant, which is the electrostatic condition on the potential inside a conductor. This condition is achieved by minimizing the total potential energy for our dynamical system,

$$U_e^{\text{tot}} = U_c - \sum_j V_j^0 q_j, \quad (5)$$

where the sum runs over the variable electrode charges and which includes a term which may be associated with the work done in charging the electrode from some external source. This additional term is in fact added so that minimizing this function with respect to all the variable charges simultaneously gives the constant potential condition.

Since the wall atom charges are obtained from a variational procedure, we may calculate the Coulombic contributions to the forces on the melt ions required for the MD procedure, given by

$$\mathbf{F}_i = - \frac{\partial U_e^{\text{tot}}}{\partial \mathbf{r}_i} \quad (6)$$

using “Hellmann-Feynman forces,” i.e., where the derivatives of the q_j with respect to \mathbf{r}_i are omitted, as in a Car-Parrinello-type procedure.¹⁵ Consequently, the forces on the melt ions are simply the Coulombic forces

$$\mathbf{F}_i = - \frac{\partial U_c}{\partial \mathbf{r}_i}. \quad (7)$$

In this dynamical system then, the variable electrode charges will take the “adiabatic” values appropriate for a metal responding to the instantaneous ionic positions while also maintaining the constant potential condition. That is, the wall charge values will account for the polarization of the electrode by the melt ions, and the melt ions themselves will follow trajectories determined by the Coulomb interactions between all charges in the system (in addition to short-range forces we describe below).

In our application the full system consists of two infinite parallel planar electrodes enclosing a set of melt ions, which is achieved within an orthorhombic simulation cell periodically replicated in the x and y directions. As such, the Coulomb energy [Eq. (3)] is expressed through a two-dimensional Ewald summation for a mixture of point and Gaussian charge distributions for which we obtain the expression in Appendix A. The derivation follows that of de Leeuw and Perram¹⁶ with help from Ref. 17 for the Gaussian integrals. The final expression is given in the efficient form obtained by Kawata and Mikami¹⁸ for the two-dimensional case. The resulting expression for the electrostatic potential felt by an electrode atom j is given by the partial derivative of this total energy with respect to the charge of an electrode atom:

$$\begin{aligned}
V_j = & \sum_i^{n_p} q_i \sum_{k=-\infty}^{\infty} \sum_{l=-\infty}^{\infty} \frac{1}{r_{ijkl}} \operatorname{erfc}(r_{ijkl}\gamma) + \sum_i^{n_g} q_i \sum_{k=-\infty}^{\infty} \sum_{l=-\infty}^{\infty} \frac{1}{r_{ijkl}} \operatorname{erfc}(\beta r_{ijkl}) + \frac{2}{ab} \sum_{k=-\infty}^{\infty} \sum_{l=-\infty}^{\infty} \int_{-\infty}^{\infty} \frac{1}{4\pi^2|\mathbf{k}|^2 + h^2} \\
& \times \exp\left(-\frac{4\pi^2|\mathbf{k}|^2 + h^2}{4\alpha^2}\right) S(\mathbf{k}, h) \exp[\iota(2\pi\mathbf{k} \cdot \mathbf{r}'_j + h z_j)] \exp\left(-\frac{4\pi k^2 + h^2}{4\eta^2}\right) dh - \frac{2}{ab} \sum_i^{n_p} q_i \left\{ \frac{\sqrt{\pi}}{\gamma} \exp(-z_{ij}^2 \gamma^2) + z_{ij} \pi \operatorname{erf}(z_{ij} \gamma) \right\} \\
& - \frac{2}{ab} \sum_i^{n_g} q_i \left\{ \frac{\sqrt{\pi}}{\beta} \exp(-z_{ij}^2 \beta^2) + z_{ij} \pi \operatorname{erf}(z_{ij} \beta) \right\} - \frac{2\beta q_j}{\sqrt{\pi}} + \frac{\sqrt{2} q_j \eta}{\sqrt{\pi}}, \quad (8)
\end{aligned}$$

where $\beta = \eta\alpha(\eta^2 + 2\alpha^2)^{-1/2}$, $\gamma = \eta\alpha(\eta^2 + \alpha^2)^{-1/2}$, and the structure factor has been redefined as

$$\begin{aligned}
S(\mathbf{k}, h) = & \sum_{i=1}^{n_p} q_i \exp[\iota(2\pi\mathbf{k} \cdot \mathbf{r}'_i + h z_i)] \\
& + \exp\left(-\frac{4\pi^2 k^2 + h^2}{4\eta^2}\right) \\
& \times \sum_{j=1}^{n_g} q_j \exp[\iota(2\pi\mathbf{k} \cdot \mathbf{r}'_j + h z_j)] \quad (9)
\end{aligned}$$

with $\mathbf{r}'_i = (x_i, y_i)$. Equation (8) is very similar to the usual Coulombic potential within Kawata and Mikami's two-dimensional Ewald summation method. The only significant differences are the duplication of terms due to the different charge distributions on melt ions and electrode atoms and the redefinition of the structure factor for the same reason. There is also an extra self-interaction (involving η) since the charge in a Gaussian charge distribution will interact with itself.

The self-consistent minimization of U_e^{tot} with respect to the variable charge values is conveniently achieved through a conjugate-gradient procedure, as described in Ref. 19, where we exploit the fact that U_e^{tot} is quadratic in the variable charges.²⁰

III. COMPARISON OF THE MODEL ELECTRODE WITH CLASSICAL ELECTROSTATICS

In this section we will discuss the comparison of the results obtained with the model system with those obtained from classical electrostatics. These comparisons are important as they enable us to confirm that the “electrode potentials” V_j^0 introduced into our model system do behave as the applied potentials in a macroscopic system and control the energies of charges introduced onto the electrodes.

Throughout, we will use a system containing two model electrodes arranged as parallel plates separated by a distance $d = 52.9$ Å. The electrodes each consist of three layers of atoms carrying variable charges arranged in the fcc lattice with the (111) face exposed. The lattice parameter used was 3.9 Å, which is that of platinum. Each electrode contained 2700 atoms so that the complete simulation cell has dimensions of $a = 83.1$ Å, $b = 72.0$ Å, and $c = 61.7$ Å. The variable charge Gaussian width parameter η was set at 0.5052 Å, the choice of which we will discuss below. The Ewald smearing

parameter α was 0.0878 Å, and the reciprocal space sums were truncated after 34, 29, and 25 terms in the x , y , and z directions, respectively. A potential difference of $2V_0$ is applied across the cell by setting one wall to $+V_0$ and the other to $-V_0$, and the value of the charge induced on the two walls determined.

The system consists of an ideal, infinite, parallel plate capacitor for which we can obtain standard results from classical electrostatics. The charge induced on the positive plate is

$$Q = \frac{\epsilon_0 A 2V_0}{d}, \quad (10)$$

where A is the area of the electrode. Minimizing Eq. (5) with respect to electrode charges q_j for an applied potential difference of $\Delta V_0 = 2V_0 = 1.1$ V gives induced charges of $-2.36 \times 10^{-4}e$, $-1.2691 \times 10^{-2}e$, and $0.696715e$ on the outer, middle, and innermost layers of the positive electrode, respectively. The corresponding layers on the negative wall carry charges of the same magnitude but opposite signs. The total induced charge on each plate is therefore $\pm 0.6838e$, which compares very well with the value of $0.6826e$ given by Eq. (10) with the appropriate geometric parameters. The majority of the charge is thus carried on the surfaces of the electrodes as predicted by the fact that the electric field within an ideal conductor is zero. During the minimization for determining the induced charge, no constraint is applied to the total system charge. In the current test case, the total charge is about $-7 \times 10^{-9}e$, which is less than the convergence criteria used in the minimization loop and in the Ewald summation.

Next, we place a particle with a charge of $-e$ halfway between the two electrodes ($z = c/2$) and at $x = y = 0$ in order to examine the induced charge distributions. For a single ideal metallic electrode, the charge distribution induced by a single point charge q at a height h above the image plane is

$$\sigma(x, y) = \frac{q'h}{2\pi(x^2 + y^2 + h^2)^{3/2}}, \quad (11)$$

where q' and h are the induced charge and the height of the real charge above the image plane. This expression is obtained by considering the potential due to point and image charges and noting that the electric field just above the electrode surface is perpendicular to the surface and is thus mi-

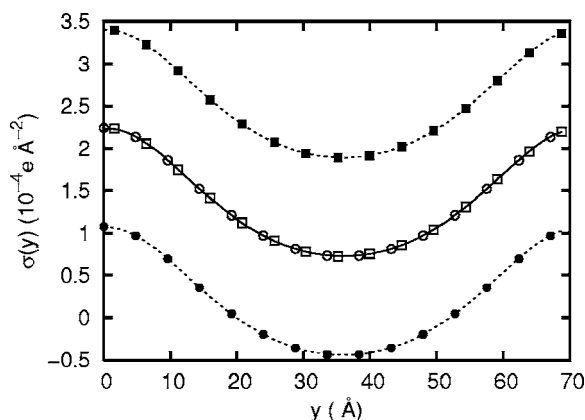


FIG. 1. Induced charge distribution along the line $x=0$ on the two surface layers (squares and circles) of the electrodes due to a point charge at $(0,0,d/2)$. The open symbols are for $\Delta V_0=0$ and the filled symbols are for $\Delta V_0=1.1$ V. Applying the potential difference shifts the distributions by $\pm\sigma_{\text{cap}}$, which is the amount of charge induced on an empty capacitor by the same potential difference. The lines are least squares fits of Eq. (12) to the data points with $q'=(0.99\pm0.01)e$, $h=(25.8\pm0.1)$ Å, $b=(71.98\pm0.02)$ Å, and $A\sigma_0=(-0.24\pm0.01)e$ where $A=5980.4$ Å² is the surface area of the electrode. From the geometry of the cell, we would expect $h=26.45$ Å and $b=71.97$ Å. $A\sigma_{\text{cap}}$ was $0.67e$.

thus the partial derivative of the potential with respect to z . The charge density is then given by ϵ_0 multiplied by the electric field. For our system we need to generalize this because the periodic boundary conditions mean that our charge at $(0,0)$ has periodic replicas at $(0\pm na, 0\pm mb)$, which will also contribute to the induced charge distribution. Confining attention to the nearest images we obtain

$$\sigma_p(y) = \sigma(0,y) + \sigma(0,y-b) + 2\sigma(a,y) + 2\sigma(a,y-b) + \sigma_0 \quad (12)$$

for the values of the induced charges along the line $x=0$. σ_0 appears due to the fact that we are considering two parallel plates rather than a single plate, and represents a background image charge induced by the net charge on the other electrode. In Fig. 1 we plot the values obtained with $\Delta V_0=0$ for the charges on the atoms in the top layers along the line $x=0$ and compare them with the values predicted by Eq. (12). The comparison is made by fitting Eq. (12), allowing variation of the induced charge q' , the height h above the image plane, and the value of σ_0 . As we increase the number of neighbors considered, we find that $h \rightarrow d/2$. In other words, the effective image planes are through the centers of the innermost layers of atoms within the electrodes. We also find that σ_0 is tending to $-q'/2A$ as we generalize Eq. (12) to include more periodic replicas, which is consistent with the interpretation given for σ_0 above. For example, including the 230 nearest replicas gives $A\sigma_0=(-0.4594\pm0.0003)e$. It is interesting to note that adding a second wall changes the induced charge density by a constant amount across the whole electrode.

By applying a potential difference, $\Delta V_0=1.1$ V, as well as imposing the test charge, the induced charge distributions on the positive and negative electrodes are shifted by an amount equal to the charge density on the plates of a capacitor with the same applied potential difference but without the test charge, see Fig. 1.

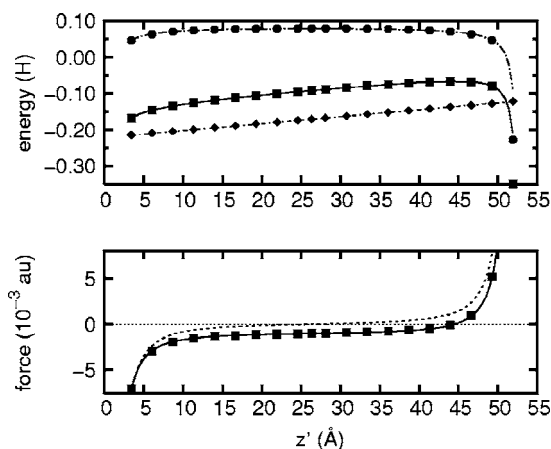


FIG. 2. (Top) Variation of energy as the test charge is moved across the cell. U_e^{tot} : squares, U_c : circles, and $-\sum V_j^0 q_j$: diamonds. Fits are to energy according to the method of images (U_c), work done against a constant electric field ($-\sum V_j^0 q_j$), and their sum ($U_c - \sum V_j^0 q_j$). See text for more details. (Bottom) Variation of the force in the z direction experienced by the test charge. The solid line is given by the method of images plus the electric field. The dashed line is for the method of images only.

We now consider the behavior of the total energy as the point charge is moved from one electrode to the other with a potential difference of 1.1 V applied across the cell. Figure 2 shows the variation of U_e^{tot} , U_c , and $-\sum V_j^0 q_j$ as the test charge is moved across the cell. Interestingly the work done in moving the test charge against the electric field is given by the change in $-\sum V_j^0 q_j$, while the work done against the image charge is given by the change in U_c . This is shown by the linear nature of $-\sum V_j^0 q_j$ and the fact that it has a gradient of $\Delta V_0/d$, which is the electric field strength. U_c is symmetrical about the center of the cell, indicating that it is not affected by the applied potential difference. U_c may be obtained directly from the method of images and the energy of an ideal capacitor using

$$U_c^{\text{theory}} = \frac{q}{4z'} + \frac{q}{4(d-z')} + U_{\text{cap}}, \quad (13)$$

where U_{cap} is the energy of the capacitor without the test charge and z' is the position with respect to the surface layer of atoms in the left hand electrode. Although this equation does not include interactions of the test charge with its periodic images, it fits the calculated variation of energy very well. The energy of the capacitor U_{cap} which is obtained is 4% different from the value predicted by $Q\Delta V/2$. Including the interactions of neighbors should improve the fit particularly around the center of the cell.

The tests presented so far have been for fixed induced charge width η . The energy of the system is found to depend only weakly on the value of η . Figure 3 shows the variation of the reduced Coulomb energy for an empty capacitor ($U_c^* = U_c/2Q\Delta V$) with η . The optimum value of η is independent of system size but does depend on the surface structure. More specifically, it can be seen that the optimum value of η is inversely proportional to the square root of the area per surface atom.

Finally, since no energy is added or removed from the system, the total system energy should be conserved during a

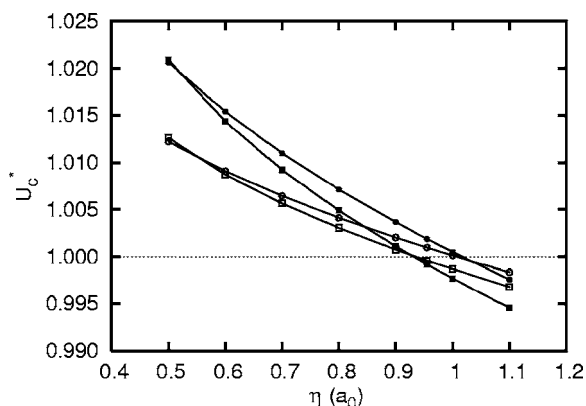


FIG. 3. Variation of energy with η for different systems. Solid squares: (001) surface comprising 800 atoms. Solid circles: (111) surfaces comprising 900 atoms. Open squares: (001) surface comprising 98 atoms. Open circles (111) surface comprising 100 atoms. The lines are simply a guide to the eyes.

MD run, and this provides a good test of our implementation of this scheme. We find that for a system containing 398 Li^+ , 398 K^+ , and 796 Cl^- ions with a total of 588 wall atoms excellent conservation is obtained. The initial total energy was $U_e^{\text{tot}} = 208.6282$ H. Fluctuations in the energy typically have a magnitude less than 5×10^{-4} H with no significant drift with time over runs of more than 100 ps in length. More details about these simulations will be given in the next section.

IV. APPLICATION TO MOLTEN SALT MIXTURES

We have applied the method to the study of two ionic liquids consisting of molten salt mixtures confined between planar metal electrodes made up of an atomic lattice with an interatomic spacing of platinum metal. In our electrodes we have included three layers of atoms from an fcc structure and with the [100] face of the crystal forming the interface with the melt. As we have seen above, the charges on the third layer are much smaller than those on the inner layer, and checks showed that including additional layers had no effect on the results for the interfacial structure and properties.

The first of these mixtures consists of an equimolar mixture of LiCl and KCl (one of the standard “solvent” systems used in molten salt electrochemistry is the eutectic mixture consisting of 59% LiCl and 41% KCl). For our purposes, it is a system chosen to exemplify the effects of an imbalance of ionic size on the interfacial structure. The crystallographic radii of the K^+ and Li^+ ions are 1.38 and 0.76 Å, respectively. The interionic interactions are represented by simple Born-Mayer pair potentials, with the ions assigned formal valence charges, and we use potentials of the same form to represent the short-range interactions with the atoms which make up the electrodes. The parameters for the LiCl and KCl interactions are the same as those used in studies of the bulk mixtures,^{21,22} and the potentials for the interactions of these ions with the atoms making up the electrode surface are obtained by imagining that the latter interact with the melt ions as if they had the same size as a Cl^- ion. In effect, these electrode-ion interactions are simply short-range repulsive interactions which respect the ion sizes. In future work we

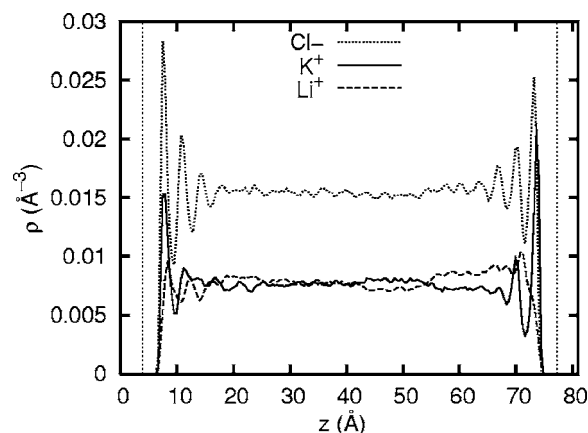


FIG. 4. Mean ion number density profiles for an applied potential of 1.63 V. The vertical lines indicate the surfaces of the electrodes.

will incorporate a more detailed representation of the “chemical” interactions between specific ions and the electrode surface and, in particular, explore the effect of the dispersion interactions between the electrolyte ions and metallic walls which may be responsible for specific absorption of ions in real systems.⁶

The second mixture we consider is introduced to allow an examination of the effect of an imbalance of cation charge on the interfacial structure, it is a mixture of 15% $\tilde{\text{M}}\text{Cl}_2$ with MCl. In practice, the interaction parameters for the M^+ and Cl^- ions in MCl consist of the standard Fumi-Tosi parameters for NaCl,²³ and we have adjusted the $\tilde{\text{M}}^{2+}-\text{Cl}$ interaction parameters so that the radial distribution functions for M^+-Cl and $\tilde{\text{M}}^{2+}-\text{Cl}$ are as similar as possible, so that in this case we minimize the effect of a change in ion size. As with the first mixture, the interaction parameters for all the interactions with the electrode atoms are modeled only crudely.

A full specification of all the interaction potentials and simulation conditions appears in Appendix B.

A. The interfacial structure for LiCl:KCl

In Fig. 4 we show the profiles of the mean ion number densities across the simulation cell under constant potential conditions. In the calculation from which the results are illustrated, the applied potential ΔV_0 was assigned a value of 1.63 V (0.06 a.u.) so that the electrode on the right-hand side of the figure is the negatively charged electrode (cathode) and the left-hand side one is positive (anode). These density profiles are obtained by dividing the interelectrode spacing into bins of width 0.4 Å and averaging the contents of the bins over the full 360 ps of the production run. As found in previous work on one component molten salts at charged walls,^{9–11} the ion density profiles are highly structured because of the packing requirements of the ions: as has been discussed previously, this oscillatory structure is not consistent with the application of the double layer ideas of electrolyte solution chemistry to the molten salt–electrode interface.

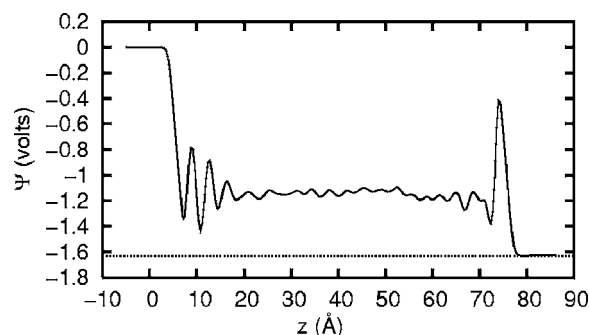


FIG. 5. Variation of the Poisson potential across the cell for $\Delta V_0=1.63$ V. The profile extends beyond the usual bounds of the simulation cell because the Gaussian charge distributions have a finite width and the outermost electrode atoms mark the limits of the cell. To get the Poisson profile, it is necessary to integrate over the whole charge density.

1. The mean electrical potential and electrode capacitance

We will return to discuss the interfacial structure in more detail below; first, we consider the behavior of the mean electrical potential across the simulation cell. This is calculated from the mean charge densities via Poisson's equation

$$\nabla^2 \Psi = -\frac{\rho}{\epsilon_0}. \quad (14)$$

Applying this equation to the mean charge densities, which are obtained from the number density profiles illustrated in Fig. 4 by multiplying with the charge on each ion, results in the potential profile shown in Fig. 5. The immediately striking aspect of this figure is the rapid screening of the potential due to the polarized electrodes by the molten salt, so that the potential is a constant beyond about 10 Å from the electrode surface. Within the electrodes, the potential is constant, as should be the case for metal electrodes. We also see that the total potential drop across the cell is 1.63 V, which confirms that the model electrode system is behaving correctly, with the potential calculated from the induced charge density equal to the external potential ($\Delta V_0=2V_0$) applied to the cell.

On closer inspection, we see that the potential differences between the electrodes and the melt in the middle of the cell are not equal, despite the fact that the electrodes are made of the same "material." This is due to the differences between the packing of the melt ions at the positive and negative electrodes. We can obtain approximate values for the capacitances of the individual positive and negative electrodes by combining the values of these potential drops with the values of the average charge density (i.e., the sum of the q_i 's) induced on the electrodes under the constant potential condition. This capacitance reflects that of an effective parallel plate capacitor for which one plate is the electrode and the other "plate" is a virtual one which carries the net charge of the screening layer induced in the electrolyte. Since we see perfect screening of the electrode charge in the bulk of the melt, it is clear that the screening charge is equal in magnitude and opposite in sign to the charge on the electrode. The calculation is performed as if the full potential drop between the electrode and the bulk melt occurs between the electrode surface and the plate carrying the screening

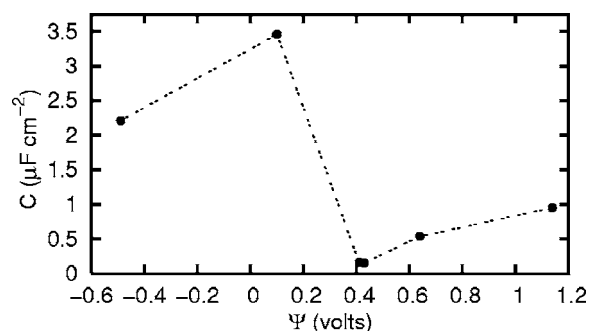


FIG. 6. Variation of electrode capacitance with potential difference between the bulk melt and the electrode, taking the bulk melt value as the reference point. The line is a guide to the eyes.

charge density; as Fig. 5 makes clear, this is a crude assumption and it would be better to model the capacitance of the screening density as a series of capacitors connected in series.

In a recent work, Kiszka²⁴ notes that the literature contains a wide range of values spanning two orders of magnitude for the double layer capacitance. He then reports the results of measuring the double layer capacitance for a mixture of MgCl_2 and several alkali chlorides using alternating potentials with a broad range of frequencies. Most noteworthy is perhaps the value of $3.35 \mu\text{F cm}^{-2}$, which he reports for a 1:4 mixture of MgCl_2 and KCl . While obviously not the same as the system studied in the present work, it is probably the most comparable. Above we have discussed how the larger K^+ ions get significantly closer to the electrode than the smaller Li^+ ions. Also, below we see that in the $\tilde{\text{MCl}}_2:\text{MCl}$ system, the singly charged cation gets closer to the electrode than the doubly charged cation. We would therefore expect that for a 1:4 mixture of MgCl_2 and KCl , the K^+ ions will significantly outnumber the Mg^{2+} ions at the electrode. The capacitance will therefore be dominated by the K^+ ions. Figure 6 therefore shows an excellent agreement with experiment.

Liu *et al.*²⁵ studied the variation of the capacitance with potential for several molten salt mixtures at inert electrodes, including $\text{LiCl}:\text{KCl}$ at platinum. They reported that the variation of capacitance with potential has a similar shape and discontinuity to that seen in Fig. 6, and noted that such discontinuities occur at the potential of zero charge. With an applied potential difference across the cell of 0 V, we find that the potential of the electrodes is about 0.4 V higher than the bulk melt, which gives an approximate value for the potential of zero charge in our system. From the figure this is seen to be the location of the discontinuity we observe in the capacitance, in agreement with the experimental observations. Unfortunately, the actual values of the capacitances reported in this work²⁵ are at least ten times larger than that reported by Kiszka²⁴ in his recent work for similar systems, and larger than our values by the same amount. The difficulties of measuring capacitances in these systems are discussed in Ref. 26. Further experimental work would be very helpful to eliminate these ambiguities and to examine how well our classical model of the electrode polarization reflects the reality.

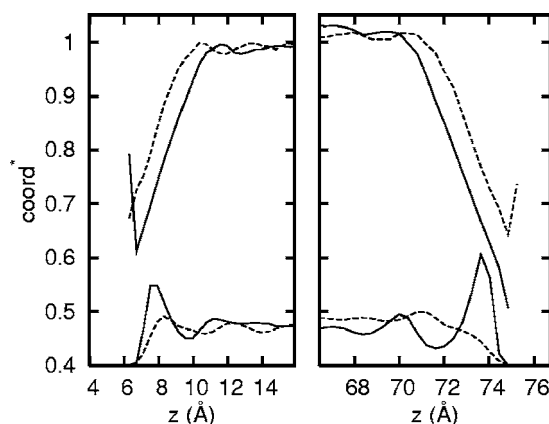


FIG. 7. Variation of the coordination numbers normalized by the bulk values (upper two lines) for the K^+ (solid line) and Li^+ (dashed line) ions. The bulk values are 7.6 and 4.1 for K^+ and Li^+ , respectively. The density profiles (lower two lines) for K^+ and Li^+ are also shown for comparison but without a y axis.

2. Ion density profiles

We return now to a more detailed consideration of the ion density profiles appearing in Fig. 4 and note that, from Fig. 5, these are appropriate to electrodes polarized by about ± 1 V with respect to the melt, i.e., typical conditions for a working electrochemical cell. Under these conditions, the average induced charge q_j on each of the atoms making up the first layer of the electrode surface is about $-0.018e$ on the cathode and $0.018e$ on the anode. At this level of polarization, there are substantial numbers of Cl^- ions in the first layer of melt ions at both the anode and cathode. What is somewhat surprising is that K^+ ions overwhelmingly outnumber Li^+ ions in these first layers, and to a greater extent at the cathode than the anode. It might have been thought that the smaller Li^+ ion would predominate at the cathode, since it can approach the negatively charged electrode ions more closely than the larger K^+ ion, and that it might even experience a greater attraction to both walls, since it can get closer to its own image charge. That the reverse happens can be attributed to the relative strength of the coordination of the two cations by the Cl^- ions. For a cation to approach the wall closely, it must shed some anions from its coordination shell (in effect, it replaces anions from the melt with the atoms of the wall). Since the wall atoms carry only small charges compared to the anions of the melt, the Li^+ ions, which are more tightly coordinated to the Cl^- ions than are the K^+ ions by virtue of their smaller size, prefer to remain in the bulk where they can retain their coordination shells intact. We confirm this explanation in Fig. 7, where we show the profiles of the mean coordination numbers for the Cl^- ions around the cations as a function of position across the cell. To facilitate the comparison, we have “normalized” the coordination numbers by their bulk values. What the figure shows is that the Li^+ ions hang on to their full coordination shells until they have approached the walls very closely, whereas the coordination shells around the K^+ ions become disrupted at relatively large distances from the wall.

A further feature of the distribution of ions in the first layer adjacent to the electrode walls is the shift in the relative position of the peaks in the Cl^- and K^+ distributions at the

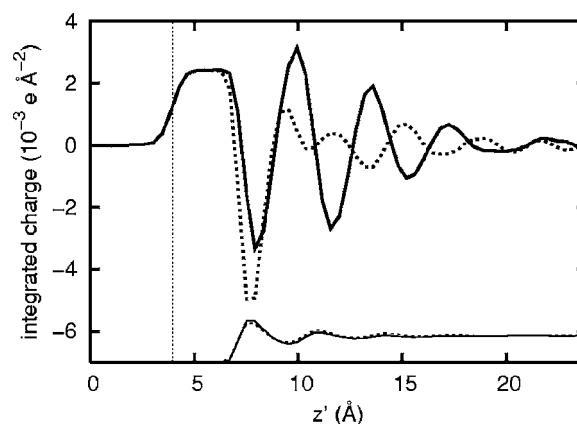


FIG. 8. The running integrals of the mean charge densities $\rho_q(z)$ from within the electrodes into the electrolyte for an applied potential of $\Delta V=1.63$ V: the thick solid and dotted lines show the anode and minus the cathode values, respectively. The vertical line indicates the position of the top layer of atoms in the electrode. The integrated charge density continues to rise after this position as the electrode atoms have Gaussian charge distributions with finite widths. Beyond about 20 Å, the integrals approach zero indicating that the electrode is completely screened. The thin curves indicate the corresponding total number densities of the electrolyte at the two electrodes for comparison.

positively and negatively charged electrodes. At the anode, the peaks of the two distributions are almost coincident, but at the cathode the K^+ peak has been moved towards the electrode, presumably drawn in by the small negative charges on the wall ions. It is due to the differences in the ionic distributions at the two electrodes, and their consequences for the mean electrical potential, that the potential drop between the two electrodes and the bulk value are not equal in magnitude (Fig. 5). This is reflected in the asymmetry of the potential dependence of the capacitance about the potential of mean charge (Fig. 6). In order to illustrate the different screening behaviors at the two electrodes, we show in Fig. 8 the running integrals of the charge density from the interior of the electrodes into the electrolyte. We reverse the sign of the integral which starts within the cathode to aid comparison. Note that the running integrals are equal until the electrolyte is reached, indicating that the mean total charge on the electrodes are equal and opposite. Also note that the running integrals return to zero showing perfect screening of the electrode charge. However, within the screening layers the distribution of charge is very different and this results in the different forms for the electrical potential at the two electrodes.

One question about these ion distributions which needs to be considered is the extent to which they are influenced by the application of the constant potential, metallic model to the electrodes, as opposed to the constant charge model used in previous simulations. To address this, we carried out equivalent simulations but with a constant charge model for the electrodes. To be specific, we determined the average charge on the atoms in each layer of the electrodes in constant potential simulations with a given applied potential ΔV_0 . (For $\Delta V_0=1.63$ V, the average charges on atoms in the outer, middle, and inner layers of the positive electrode are $-0.000\,08e$, $0.000\,37e$, and $0.018\,49e$, respectively. The corresponding layers of the negative electrode carry charges of

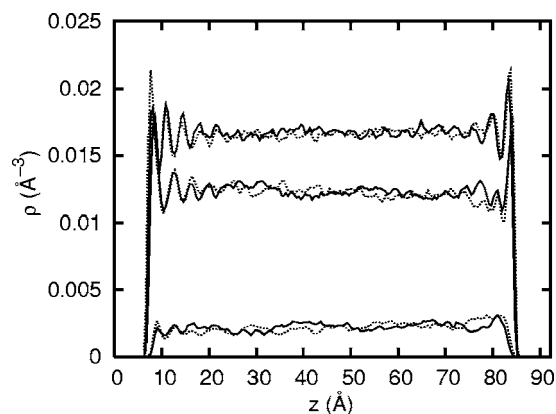


FIG. 9. Mean ion number density profiles for $\tilde{\text{MCl}}_2:\text{MCl}$ with an applied potential of 1.9 V. Solid line: constant potential electrodes, dotted line constant charge electrodes. Top profile: Cl^- ions, middle: M^+ ions, and bottom: $\tilde{\text{M}}^{2+}$.

equal magnitude, to this precision, but opposite sign; see Fig. 8.) We then set up a constant charge model, with exactly the same initial atomic arrangement for the electrodes as used in the constant potential simulations, and assigned fixed charges with values equal to the mean charges from the constant potential calculations so as to match the two electrode models as closely as possible. Any differences between the ionic behavior observed in the two simulations would therefore be due to the dynamic nature of the image charges in the constant potential calculations, which allows for local fluctuations in the image charges on the electrodes in response to a local fluctuation of the ion densities in the melt. The mean contribution of the image charges to the charging of the electrode are included in the constant charge model. We then ran simulations of comparable lengths to the previously discussed constant potential simulations. For the $\text{LiCl}:\text{KCl}$ mixture we found no discernible difference between the ionic density profiles in the two simulations. We will discuss another system, for which this is not the case, below.

B. The interfacial structure for $\tilde{\text{MCl}}_2:\text{MCl}$

We have carried out a similar series of calculations on the second molten salt mixture consisting of a 15% solution of $\tilde{\text{MCl}}_2$ in MCl , where the cation-chloride interaction potentials have been tuned to give a very similar coordination shell structure for the anions around the cations. Apart from the interest in the consequences of the charge asymmetry for the interfacial structure, we will, in future work, use this system as a model for examining the kinetics of electron transfer between the electrodes and a redox couple in which $\tilde{\text{M}}^{2+}$ and M^+ are regarded as two oxidation states of the same element. As such, our interest is focused on the ion densities in the immediate vicinity of the electrodes, where such electron transfer processes are likely to occur.

Results for the ion density profiles from constant potential simulations with an applied potential $\Delta V_0 = 1.9$ V are shown in Fig. 9 and are compared with the profiles obtained from constant charge electrodes, where the fixed charges have been chosen to match the average charges in the constant potential simulations, as above. In contrast to the

$\text{LiCl}:\text{KCl}$ mixtures, we now see a difference between the two simulations with regard to the ionic profiles, which is most pronounced in the profiles for the $\tilde{\text{M}}^{2+}$ ion at the cathode (the right-hand side of the figure). As in the $\text{LiCl}:\text{KCl}$ case, the ion which would naively be expected to approach the negatively charged electrode most closely (i.e., the doubly charged $\tilde{\text{M}}^{2+}$) is, in fact, repelled from it. The reason is the same as we discussed above in the $\text{LiCl}:\text{KCl}$ case: the $\tilde{\text{M}}^{2+}$ ion is very reluctant to release its coordinating Cl^- ions in order to approach the wall. This effect could have a very significant influence on the kinetics of electron transfer reactions involving such multiply charged ions since, in order to undergo an electron transfer reaction with the electrode, the ion must approach very closely to be within the range at which electrons may tunnel out from the electrode into the melt. It appears from the simulations that the $\tilde{\text{M}}^{2+}$ ion more readily approaches the electrode surface in the constant charge simulations. Although the effect is not large, even small changes in the distance of closest approach could be of practical significance because tunneling currents decay exponentially with distance.

V. CONCLUSIONS

We have shown that the model metallic electrode system can be implemented in such a way as to allow large-scale, long-running MD simulations which will allow direct comparison with electrochemical measurements. The electrical potentials acting on the ions are calculated from the charges present in the simulated system but may be related to the externally applied potential. The charges on the electrode atoms are calculated within the model to be consistent with the constant potential model, rather than being prescribed. As such, image charge effects are included and, furthermore, nonplanar electrode geometries become possible. The implementation conserves energy sufficiently well to allow reliable data on the energies of single ions to be extracted from the simulations and, as we shall show in subsequent work, to model electron transfer processes within the Marcus description.

In the present work we have applied the model to study the local structure in the vicinity of the electrode surfaces in ionic liquids consisting of binary molten salt mixtures with a common anion. The objective was to examine how asymmetry in the cation size or in the cation charge affects the interfacial structure. The relative strength of the interaction of the two cations with the anions was found to have a dramatic effect on the ability of a cation to approach the electrode. The more strongly coordinated cation is unable to approach the electrode surface closely, even the negatively charged one. This effect is reminiscent of the consequences of the strong hydration of small cations in aqueous solutions.

APPENDIX A: DERIVATION OF COULOMB ENERGY

The Coulomb energy of a system which is periodic in two dimensions is

$$U_c = \frac{1}{2} \sum_{i,j} \sum_{\mathbf{k}, \mathbf{l}=-\infty}^{\infty} \int \int \frac{\rho_i(\mathbf{r}') \rho_j(\mathbf{r}'') d\mathbf{r}' d\mathbf{r}''}{|\mathbf{r}_{ij} + \mathbf{r}'' - \mathbf{r}' + \mathbf{k}\mathbf{a} + \mathbf{l}\mathbf{b}|}, \quad (\text{A1})$$

where ρ_i is the charge distribution associated with particle i , $\mathbf{r}_{ij} = \mathbf{r}_i - \mathbf{r}_j$, and \mathbf{a} and \mathbf{b} are elementary lattice vectors in the periodic directions.

In the system we are currently interested in, some of the particles (the melt ions) have point charge distributions while the others (electrode atoms) have Gaussian charge distributions. The following derivation for the Ewald summation for such a mixed system is performed along the lines of the derivation for a system of pure point charges by de Leeuw and Perram.¹⁶ Some of the procedure, however, makes use of

the Gaussian integrals in the Appendix of Ref. 17, while the final form is obtained with help from the work of Kawata and Mikami.¹⁸

Equation (A1) may be split into three parts. The first part gives the Coulomb energy of the point charge subsystem, the second part gives the energy of the subsystem with Gaussian charge distributions, while the third and final part gives the interaction energy of the point charges interacting with the Gaussian charge distributions. The first part is clearly the same as the result found previously.^{16,18} The derivation of the third part is essentially the same as but slightly less complicated than the derivation of the second part. We therefore restrict our proof to that for a pure Gaussian system but give the general result for the mixed system at the end.

The Gaussian charge density for a particle is given by Eq. (1). Incorporating this into Eq. (A1) gives

$$U_c = \frac{A^2}{2} \sum_{i,j} \sum_{\mathbf{k}, \mathbf{l}=-\infty}^{\infty} \int \int \frac{q_i \exp(-|\mathbf{r}' - \mathbf{r}_i|^2 \eta^2) q_j \exp(-|\mathbf{r}'' - \mathbf{r}_j|^2 \eta^2) d\mathbf{r}' d\mathbf{r}''}{|\mathbf{r}_{ij} + \mathbf{r}'' - \mathbf{r}' + \mathbf{k}\mathbf{a} + \mathbf{l}\mathbf{b}|}. \quad (\text{A2})$$

We then use the identities

$$r^{-1} = \frac{1}{\sqrt{\pi}} \int_0^\infty t^{-1/2} \exp(-r^2 t) dt, \quad (\text{A3})$$

$$\exp(-z^2 t) = \frac{1}{2\sqrt{\pi t}} \int_{-\infty}^\infty \exp\left(-\frac{u^2}{4t} + u z\right) du, \quad (\text{A4})$$

and

$$\exp(-|\mathbf{r}|^2 \eta^2) = (2\pi)^{-3} \frac{\pi^{3/2}}{\eta^3} \int_{-\infty}^\infty \exp\left(-\frac{|\mathbf{v}|^2}{4\eta^2} + \mathbf{v} \cdot \mathbf{r}\right) d\mathbf{v}, \quad (\text{A5})$$

and Jacobi's imaginary transformation,

$$\begin{aligned} \sum_{k=-\infty}^{\infty} \exp[-(x + ka)^2 t] \\ = \frac{1}{a} \left(\frac{\pi}{t}\right)^{1/2} \sum_{k=-\infty}^{\infty} \exp\left[-\frac{\pi^2 k^2}{a^2 t} + \frac{i2\pi kx}{a}\right], \end{aligned} \quad (\text{A6})$$

with $\iota = \sqrt{-1}$ to get

$$\begin{aligned} U_c = \frac{1}{4ab(2\pi)^6} \sum_{i,j} q_i q_j \sum_{\mathbf{k}=-\infty}^{\infty} \sum_{\mathbf{l}=-\infty}^{\infty} \int t^{-2} \\ \times \exp\left[-\frac{\pi^2 k^2}{a^2 t} + \frac{i2\pi k}{a}(x'' + x_{ij} - x')\right] \\ \times \exp\left[-\frac{\pi^2 l^2}{b^2 t} + \frac{i2\pi l}{b}(y'' + y_{ij} - y')\right] \end{aligned}$$

$$\begin{aligned} & \times \exp\left[-\frac{u^2}{4t} + u(z'' + z_{ij} - z')\right] \\ & \times \exp\left(-\frac{|\mathbf{v}|^2}{4\eta^2} + \mathbf{v} \cdot \mathbf{r}'\right) \\ & \times \exp\left(-\frac{|\mathbf{w}|^2}{4\eta^2} + \mathbf{w} \cdot \mathbf{r}''\right) du dv dw dt d\mathbf{r}' d\mathbf{r}'' \end{aligned} \quad (\text{A7})$$

Next collecting terms with single and double primes and noting that, for example,

$$(2\pi)^{-1} \int \exp\left[\iota x' \left(v_x - \frac{2\pi k}{a}\right)\right] dx' = \delta\left(v_x - \frac{2\pi k}{a}\right), \quad (\text{A8})$$

where δ is the Kronecker delta function,¹⁷ we get

$$\begin{aligned} U_c = \frac{1}{4ab} \sum_{i,j} q_i q_j \sum_{\mathbf{k}=-\infty}^{\infty} \sum_{\mathbf{l}=-\infty}^{\infty} \int t^{-2} \exp\left(-\frac{|\mathbf{v}|^2 + |\mathbf{w}|^2}{4\eta^2}\right) \\ \times \exp\left[-\frac{\pi^2 k^2}{a^2 t} + \frac{i2\pi kx_{ij}}{a}\right] \exp\left[-\frac{\pi^2 l^2}{b^2 t} + \frac{i2\pi ly_{ij}}{b}\right] \\ \times \exp\left[-\frac{u^2}{4t} + u z_{ij}\right] \delta\left(v_x - \frac{2\pi k}{a}\right) \delta\left(v_y - \frac{2\pi l}{b}\right) \\ \times \delta(v_z - u) \delta\left(w_x + \frac{2\pi k}{a}\right) \delta\left(w_y + \frac{2\pi l}{b}\right) \\ \times \delta(w_z + u) du dv dw dt \end{aligned} \quad (\text{A9})$$

Integrating with respect to \mathbf{v} and \mathbf{w} over the delta func-

tions chooses: $v_x = 2\pi k/a$, $v_y = 2\pi l/b$, $v_z = u$, $w_x = -2\pi k/a$, $w_y = -2\pi l/b$, and $w_z = -u$. On rearrangement, this gives

$$U = \frac{1}{4ab} \sum_{i,j} q_i q_j \sum_{k=-\infty}^{\infty} \sum_{l=-\infty}^{\infty} \int_{t=0}^{\infty} \int_{u=-\infty}^{\infty} t^{-2} \times \exp \left[-\frac{\pi^2 k^2}{a^2} \left(\frac{1}{t} + \frac{2}{\eta^2} \right) + \frac{i2\pi k x_{ij}}{a} \right] \times \exp \left[-\frac{\pi^2 l^2}{b^2} \left(\frac{1}{t} + \frac{2}{\eta^2} \right) + \frac{i2\pi l y_{ij}}{b} \right] \times \exp \left[-\frac{u^2}{4} \left(\frac{1}{t} + \frac{2}{\eta^2} \right) + u z_{ij} \right] du dt. \quad (\text{A10})$$

Next we split the integral over t into two parts, from 0 to α^2 and from α^2 to ∞ . To begin with, consider only the upper part. After reversing the Jacobi transformations and the identity from Eq. (A4) and making a change of variable $v^2 = r^2 t \eta^2 / (\eta^2 + 2t)$, we arrive at

$$U_I = \frac{1}{2} \sum_{i,j} q_i q_j \sum_{k=-\infty}^{\infty} \sum_{l=-\infty}^{\infty} \frac{1}{r_{ijkl}} \frac{2}{\sqrt{\pi}} \int_{v_0^2}^{\infty} \exp(-v^2) dv, \quad (\text{A11})$$

where $r_{ijkl} = \{(x_{ij} + ka)^2 + (y_{ij} + lb)^2 + z_{ij}^2\}^{1/2}$. The complimentary error function is defined as

$$\text{erfc}(v_0) = \frac{2}{\sqrt{\pi}} \int_{v_0^2}^{\infty} \exp(-v^2) dv, \quad (\text{A12})$$

so the final expression for the contribution of the upper part of the integral to the energy is

$$U_I = \frac{1}{2} \sum_{i,j} q_i q_j \sum_{k=-\infty}^{\infty} \sum_{l=-\infty}^{\infty} \frac{1}{r_{ijkl}} \text{erfc}(r_{ijkl}\beta), \quad (\text{A13})$$

where $\beta = \eta\alpha(\eta^2 + 2\alpha^2)^{-1/2}$. In practice, the parameter α is usually chosen so that the complimentary error function has decayed to zero within half the length of the smallest dimension of the system, in which case the sum over k and l may be ignored.

Now we consider the lower part of the integral over t in Eq. (A10). The integral with respect to t diverges when $k=l=0$. This term can be subtracted and then added separately:

$$U_{II} = \frac{1}{4ab} \sum_{i,j} q_i q_j \sum_{k=-\infty}^{\infty} \sum_{l=-\infty}^{\infty} \int_{t=0}^{\alpha^2} \int_{u=-\infty}^{\infty} t^{-2} \times \exp \left[-i2\pi \left(\frac{kx_{ij}}{a} + \frac{ly_{ij}}{b} \right) \right] \exp(uz_{ij}) \times \exp \left[-\left(\frac{\eta^2 + 2t}{\eta^2 t} \right) \left(\frac{\pi^2 k^2}{a^2} + \frac{\pi^2 l^2}{b^2} + \frac{u^2}{4} \right) \right] du dt + \frac{1}{4ab} \sum_{i,j} q_i q_j \int_{t=0}^{\alpha^2} \int_{u=-\infty}^{\infty} t^{-2} \times \exp \left[-\frac{u^2}{4} \left(\frac{\eta^2 + 2t}{\eta^2 t} \right) + uz_{ij} \right] du dt, \quad (\text{A14})$$

where the prime indicates that the $k=l=0$ term is excluded from the summation. After removing the identity of Eq. (A4), the $k=l=0$ term in Eq. (A14) may be written as

$$U_{II}^0 = \frac{\sqrt{\pi}}{2ab} \sum_{i,j} q_i q_j \int_{t=0}^{\alpha^2} t^{-2} \left(\frac{t\eta^2}{\eta^2 + 2t} \right)^{1/2} \times \exp \left[-z^2 \frac{t\eta^2}{\eta^2 + 2t} \right] dt. \quad (\text{A15})$$

Changing the variable again in a similar way as before gives

$$U_{II}^0 = \frac{\sqrt{\pi}}{ab} \sum_{i,j} q_i q_j \int_0^{u_a^2} \frac{1}{u^2} \exp(-z_{ij}^2 u^2) du. \quad (\text{A16})$$

This can be integrated by parts to get

$$U_{II}^0 = \frac{-\sqrt{\pi}}{ab} \sum_{i,j} q_i q_j \left\{ \frac{\sqrt{\eta^2 + 2\alpha^2}}{\eta\alpha} \exp \left(-\frac{z_{ij}^2 \eta^2 \alpha^2}{\eta^2 + 2\alpha^2} \right) + z_{ij} \sqrt{\pi} \text{erf} \left(\frac{z_{ij} \eta \alpha}{\sqrt{\eta^2 + 2\alpha^2}} \right) + \lim_{t \searrow 0} \frac{\sqrt{2 + \eta^2/t}}{\eta} \right\}. \quad (\text{A17})$$

As η^2/t becomes large, the limit may be written as $\lim_{t \searrow 0} t^{-1/2}$. As this is independent of α and η , this term disappears if the system as a whole is neutral. The final expression for the U_{II}^0 is therefore

$$U_{II}^0 = \frac{-\sqrt{\pi}}{ab} \sum_{i,j} q_i q_j \left\{ \frac{1}{\beta} \exp(-z^2 \beta^2) + z \sqrt{\pi} \text{erf}(z\beta) \right\}, \quad (\text{A18})$$

where β is defined after Eq. (A13).

Finally, we return to the lower part of the integral in Eq. (A10) but when k and l are not both equal to zero. After rearranging Eq. (A10) and setting $v = t\eta^2 / (\eta^2 + 2t)$, we obtain

$$U_{II}^* = \frac{1}{4ab} \sum_{i,j} q_i q_j \sum_{k=-\infty}^{\infty} \sum_{l=-\infty}^{\infty} \int_{v=0}^{v_0} \int_{u=-\infty}^{\infty} v^{-2} \times \exp \left[i 2 \pi \left(\frac{kx_{ij}}{a} + \frac{ly_{ij}}{b} + \frac{uz_{ij}}{2\pi} \right) \right] \times \exp \left[-\frac{1}{v} \left(\frac{\pi^2 k^2}{a^2} + \frac{\pi^2 l^2}{b^2} + \frac{u^2}{4} \right) \right] du dv. \quad (A19)$$

The integral with respect to v is straightforward and we get

$$U_{II}^* = \frac{1}{4ab} \sum_{i,j} q_i q_j \sum_{k=-\infty}^{\infty} \sum_{l=-\infty}^{\infty} \exp \left[i 2 \pi \left(\frac{kx_{ij}}{a} + \frac{ly_{ij}}{b} \right) \right] \times \exp \left[-\pi \beta^2 \left(\frac{k^2}{a^2} + \frac{l^2}{b^2} \right) \right] \times \int_{-\infty}^{\infty} \frac{\exp[-(u^2/4\beta^2) + uz_{ij}]}{((\pi^2 k^2/a^2) + (\pi^2 l^2/b^2) + (u^2/4))} du. \quad (A20)$$

This is essentially Eq. (9) of de Leeuw and Perram, with $\beta^2 = \alpha^2 \eta^2 / (\eta^2 + 2\alpha^2)$ instead of α^2 . According to de Leeuw and Perram, this can then be written as

$$U_{II}^* = \frac{1}{4ab} \sum_{i,j} q_i q_j \sum_{k=-\infty}^{\infty} \sum_{l=-\infty}^{\infty} \exp \left[i 2 \pi \left(\frac{kx_{ij}}{a} + \frac{ly_{ij}}{b} \right) \right] \times \left(\frac{k^2}{a^2} + \frac{l^2}{b^2} \right)^{-1/2} F_{kl}(z_{ij}), \quad (A21)$$

where

$$F_{kl}(z_{ij}) = \exp(-2\pi|\mathbf{k}|z) \operatorname{erfc} \left(\frac{\pi|\mathbf{k}|}{\beta} - z_{ij}\beta \right) + \exp(2\pi|\mathbf{k}|z) \operatorname{erfc} \left(\frac{\pi|\mathbf{k}|}{\beta} + z_{ij}\beta \right), \quad (A22)$$

with

$$|\mathbf{k}| = \left(\frac{k^2}{a^2} + \frac{l^2}{b^2} \right)^{1/2}. \quad (A23)$$

Kawata and Mikami¹⁸ noted that this can be rewritten using a Fourier integral

$$\frac{1}{4|\mathbf{k}|} \exp \left(\frac{\pi^2 |\mathbf{k}|^2}{\beta^2} \right) \left[e^{-2\pi|\mathbf{k}|z} \operatorname{erfc} \left(\frac{\pi|\mathbf{k}|}{\beta} - \beta z_{ij} \right) + e^{2\pi|\mathbf{k}|z} \operatorname{erfc} \left(\frac{\pi|\mathbf{k}|}{\beta} + \beta z_{ij} \right) \right] = \int_{-\infty}^{\infty} dh e^{ihz_{ij}} \frac{1}{4\pi^2 |\mathbf{k}|^2 + h^2} \exp \left(-\frac{\mathbf{h}^2}{4\beta^2} \right) \quad (A24)$$

to get

$$U_{II}^* = \frac{1}{ab} \sum_{i,j} q_i q_j \sum_{k=-\infty}^{\infty} \sum_{l=-\infty}^{\infty} \exp \left[i 2 \pi \left(\frac{kx_{ij}}{a} + \frac{ly_{ij}}{b} \right) \right] \times \int_{-\infty}^{\infty} dh e^{ihz_{ij}} \frac{1}{4\pi^2 |\mathbf{k}|^2 + h^2} \exp \left(-\frac{|4\pi^2 \mathbf{k}|^2 + h^2}{4\beta^2} \right). \quad (A25)$$

Defining the structure factor $S(\mathbf{k}, h)$ as

$$S(\mathbf{k}, h) = \exp \left(-\frac{4\pi^2 k^2 + h^2}{4\eta^2} \right) \sum_i q_i \exp[i(2\pi \mathbf{k} \cdot \mathbf{r}'_i + h z_i)], \quad (A26)$$

with $\mathbf{r}'_i = (x_i, y_i)$ and $\mathbf{k} = (k/a, l/b)$, we can rewrite U_{II}^* as

$$U_{II}^* = \frac{1}{ab} \sum_{k=-\infty}^{\infty} \sum_{l=-\infty}^{\infty} \int_{-\infty}^{\infty} dh \frac{1}{4\pi^2 |\mathbf{k}|^2 + h^2} \times \exp \left(-\frac{4\pi^2 |\mathbf{k}|^2 + h^2}{4\alpha^2} \right) |S(\mathbf{k}, h)|^2. \quad (A27)$$

U_{II} erroneously includes part of the interaction of the particle with itself. This contribution, which needs to be subtracted, may be determined by considering $U - U_I$ for a single particle:

$$\frac{q_i^2}{2r} - \frac{q_i^2}{2} \lim_{r \rightarrow 0} \frac{\operatorname{erfc}(\beta r)}{r} = \frac{q_i^2 \beta}{\sqrt{\pi}}. \quad (A28)$$

For the Gaussian charge distribution, the full self-term which needs to be added is

$$U_{\text{self}} = \frac{1}{2} \int \int \frac{1}{|\mathbf{r} - \mathbf{r}'|} \frac{\eta^6}{\pi^3} \exp(-r^2 \eta^2) \exp(-r'^2 \eta^2) d\mathbf{r} d\mathbf{r}' = \frac{q_i^2 \eta}{\sqrt{2\pi}}. \quad (A29)$$

The total Coulomb energy for a system of Gaussian charge distributions is therefore

$$U_c = U_I + U_{II}^* + U_{II}^0 - \frac{q_i^2 \beta}{\sqrt{\pi}} + \frac{q_i^2 \eta}{\sqrt{2\pi}}. \quad (A30)$$

These equations are almost the same as those for a system of point charges derived previously^{16,18} apart from the redefinition of the structure factor, the Gaussian self-interaction term, and the inclusion of β rather than just α .

The derivation of the equations for the Coulomb energy of a system of point charges interacting with a system of Gaussian charges is virtually the same as for the Gaussian-Gaussian Coulomb energy except that the initial factor of 2 is not present, since as the particles have either a point or Gaussian charge distribution, there is no double counting. As one of the charge distributions becomes a delta function, one

of the integrals in Eq. (A2) disappears. Also, β becomes $\gamma = \eta\alpha(\eta^2 + \alpha^2)^{-1/2}$ and there is no self-interaction correction. The incorporation of η into the structure factor as in Eq. (A26) is not quite so clean. This is resolved, however, when we consider the complete system with both Gaussian and point charges.

The total Coulomb energy for a system comprising both point and Gaussian charges is simply the sum of the original point-point interaction terms, the Gaussian-Gaussian terms, and the cross term which is again very similar. If there are n_p point charges and n_g Gaussian charges, the final expression for the Coulomb energy is

$$\begin{aligned}
 U_c = & \frac{1}{2} \sum_{i,j}^{n_p} q_i q_j \frac{1}{r_{ij}} \operatorname{erfc}(\alpha r_{ij}) + \sum_i^{n_p} \sum_j^{n_g} q_i q_j \frac{1}{r_{ij}} \operatorname{erfc}(\gamma r_{ij}) + \frac{1}{2} \sum_{i,j}^{n_g} q_i q_j \frac{1}{r_{ij}} \operatorname{erfc}(\beta r_{ij}) + \frac{1}{ab} \sum_{k=-\infty}^{\infty} \sum_{l=-\infty}^{\infty} \int_{-\infty}^{\infty} \frac{1}{4\pi^2 |\mathbf{k}|^2 + h^2} \\
 & \times \exp\left(-\frac{4\pi^2 |\mathbf{k}|^2 + h^2}{4\alpha^2}\right) |S(\mathbf{k}, h)|^2 dh - \frac{1}{ab} \sum_{i,j}^{n_p} q_i q_j \left\{ \frac{\sqrt{\pi}}{\alpha} \exp(-z_{ij}^2 \alpha^2) + z_{ij} \pi \operatorname{erf}(z_{ij} \alpha) \right\} \\
 & - \frac{2}{ab} \sum_i^{n_p} \sum_j^{n_g} q_i q_j \left\{ \frac{\sqrt{\pi}}{\gamma} \exp(-z_{ij}^2 \gamma^2) + z_{ij} \pi \operatorname{erf}(z_{ij} \gamma) \right\} - \frac{1}{ab} \sum_{i,j}^{n_g} q_i q_j \left\{ \frac{\sqrt{\pi}}{\beta} \exp(-z_{ij}^2 \beta^2) + z_{ij} \pi \operatorname{erf}(z_{ij} \beta) \right\} \\
 & - \sum_i^{n_p} \frac{\alpha q_i^2}{\sqrt{\pi}} - \sum_i^{n_g} \frac{\beta q_i^2}{\sqrt{\pi}} + \sum_i^{n_g} \frac{\eta q_i^2}{\sqrt{2\pi}},
 \end{aligned} \tag{A31}$$

where we have redefined the structure factor again, this time as

$$S(\mathbf{k}, h) = \sum_{i=1}^{n_p} q_i \exp[u(2\pi \mathbf{k} \cdot \mathbf{r}'_i + h z_i)] + \exp\left(-\frac{4\pi^2 k^2 + h^2}{4\eta^2}\right) \sum_{j=1}^{n_g} q_j \exp[u(2\pi \mathbf{k} \cdot \mathbf{r}'_j + h z_j)], \tag{A32}$$

with $\mathbf{r}'_i = (x_i, y_i)$, $\mathbf{k} = (k/a, l/b)$, $\beta = \eta\alpha(\eta^2 + 2\alpha^2)^{-1/2}$, and $\gamma = \eta\alpha(\eta^2 + \alpha^2)^{-1/2}$. By dropping the sums over k and l for the so-called real-space terms involving α , β , and γ , it has been assumed that α is chosen so that $\operatorname{erfc}(\alpha r)$ decays to zero within half the smallest dimension of the cell.

In order to perform molecular dynamics simulations, it is necessary to have an expression for the Coulomb force on a particle, which is given by

$$\mathbf{F}_i = -\frac{\partial U}{\partial \mathbf{r}_i}. \tag{A33}$$

If particle i is one of the n_p particles which have a point charge, then the Coulomb force which it experiences is

$$\begin{aligned}
 \mathbf{F}_i = & \sum_j^{n_p} q_i q_j \left[\frac{1}{r_{ij}^2} \operatorname{erfc}(\alpha r_{ij}) + \frac{2\alpha}{r_{ij} \sqrt{\pi}} \exp(\alpha^2 r_{ij}^2) \right] \frac{\mathbf{r}_{ij}}{|\mathbf{r}_{ij}|} + \sum_j^{n_g} q_i q_j \left[\frac{1}{r_{ij}^2} \operatorname{erfc}(r_{ij} \gamma) + \frac{2\gamma}{r_{ij} \sqrt{\pi}} \exp(r_{ij}^2 \gamma^2) \right] \frac{\mathbf{r}_{ij}}{|\mathbf{r}_{ij}|} \\
 & + \frac{2q_i}{ab} \sum_{k=-\infty}^{\infty} \sum_{l=-\infty}^{\infty} \int_{-\infty}^{\infty} \frac{2\pi k \hat{x}/a + 2\pi l \hat{y}/b + h \hat{z}}{4\pi^2 |\mathbf{k}|^2 + h^2} \exp\left(-\frac{4\pi^2 |\mathbf{k}|^2 + h^2}{4\alpha^2}\right) \left[\sin(2\pi \mathbf{k} \cdot \mathbf{r}'_i + h z_i) \sum_{j=1}^{n_p} q_j \cos(2\pi \mathbf{k} \cdot \mathbf{r}_j + h z_j) \right. \\
 & + \sin(2\pi \mathbf{k} \cdot \mathbf{r}'_i + h z_i) \exp\left(\frac{-k^2}{4\eta^2}\right) \sum_{j=1}^{n_g} q_j \cos(2\pi \mathbf{k} \cdot \mathbf{r}'_j + h z_j) - \cos(2\pi \mathbf{k} \cdot \mathbf{r}'_i + h z_i) \sum_{j=1}^{n_p} q_j \sin(2\pi \mathbf{k} \cdot \mathbf{r}'_j + h z_j) \\
 & \left. - \cos(2\pi \mathbf{k} \cdot \mathbf{r}'_i + h z_i) \exp\left(\frac{-k^2}{4\eta^2}\right) \sum_{j=1}^{n_g} q_j \sin(2\pi \mathbf{k} \cdot \mathbf{r}'_j + h z_j) \right] dh + \frac{2q_i}{ab} \sum_j^{n_p} q_j \pi \operatorname{erf}(z_{ij} \alpha) \hat{z} + \frac{2q_i}{ab} \sum_j^{n_g} q_j \operatorname{erf}(z_{ij} \gamma) \hat{z},
 \end{aligned} \tag{A34}$$

where \hat{x} , \hat{y} , and \hat{z} are unit vectors in the x , y , and z directions, respectively.

The forces on particles with Gaussian charge distributions will be very similar but are not needed in the present model, since only the atoms in the electrode have Gaussian charges and their positions are fixed.

APPENDIX B: SIMULATION DETAILS

Simulations of both systems were performed at about 1300 K. Results were collected only after the systems had been equilibrated under each set of conditions. A time step of 1.2 fs was used for the trajectory integration, and results were collected over at least 360 ps. The LiCl:KCl system

TABLE I. Pair potential parameters for LiCl:KCl system. All the parameters are given in a.u.

Ion pair	B_{ij}	A_{ij}	C_{ij}^6	C_{ij}^8	b_{ij}^6	b_{ij}^8
Cl ⁻ -Cl ⁻	100.0	1.53	360	7200	1.5	1.0
Cl ⁻ -K ⁺	450.0	1.8	102.2	1000	1.5	1.51
Cl ⁻ -Li ⁺	12.42	1.56	2.09	8.95	10 ⁶	10 ⁶
Cl ⁻ -wall	100.0	1.53	100	1000	1.5	1.0
K ⁺ -K ⁺	10.0	2.80	30.0	500.0	1.90	1.80
K ⁺ -Li ⁺	450	1.8	102.2	1000.0	1.5	1.51
K ⁺ -wall	450	1.8	102.2	1000.0	1.5	1.51
Li ⁺ -Li ⁺	1.97	1.57	0.076	0.11	10 ⁶	10 ⁶
Li ⁺ -wall	12.42	1.56	2.09	8.95	10 ⁶	10 ⁶

contained 398 Li⁺, 398 K⁺, and 796 Cl⁻ ions, while the $\tilde{\text{MCl}}_2\text{:MCl}$ contained 633 M⁺, 109 $\tilde{\text{M}}^{2+}$, and 851 Cl⁻ ions. No thermostat was applied to the system. The total energy of the system includes not only the electrostatic energy but also short-range U_{sr} and dispersive U_{disp} interactions and the kinetic energy U_K . It may be written as

$$U_{\text{tot}} = U_e^{\text{tot}} + U_{\text{sr}} + U_{\text{disp}} + U_K. \quad (\text{B1})$$

The short-range contributions to the energy are given by

$$U_{\text{sr}} = \frac{1}{2} \sum_{i,j} B_{ij} \exp(-A_{ij}r_{ij}). \quad (\text{B2})$$

The dispersion is modeled using

$$U_{\text{disp}} = \frac{1}{2} \sum_{i,j} \left[\frac{C_{ij}^6}{(r_{ij})^6} f_6(r_{ij}) + \frac{C_{ij}^8}{(r_{ij})^8} f_8(r_{ij}) \right], \quad (\text{B3})$$

where f_6 and f_8 are the sixth and eighth order Tang-Toennies functions:²⁷

$$f_{n_k}(r_{ij}) = 1 - \exp(-b_{ij}^{n_k} r_{ij}) \sum_{k=0}^{n_k} \frac{(b_{ij}^{n_k} r_{ij})^k}{k!}. \quad (\text{B4})$$

The values for the interaction parameters given in Table I have been taken from previous work on bulk LiCl/KCl,^{21,22} to which we have added interactions between the melt ions and the wall.

The interaction potential parameters for the $\tilde{\text{MCl}}_2\text{:MCl}$ system have been constructed from the initial Fumi-Tosi parameters²³ for NaCl so that the $\tilde{\text{M}}\text{-Cl}$ coordination shell is very similar to that of M-Cl and, again, with crude models for the ion-wall interactions. These parameters are given in Table II.

TABLE II. Pair potential parameters for $\text{MCl}_2\text{:MCl}$ system. All the parameters are given in a.u.

Ion pair	B_{ij}	α_{ij}	C_{ij}^6	C_{ij}^8	b_{ij}^6	b_{ij}^8
Cl ⁻ -Cl ⁻	128.13	1.67	121.18	869.15	10 ⁷	10 ⁷
Cl ⁻ -M ⁺	46.14	1.67	11.70	51.85	10 ⁷	10 ⁷
Cl ⁻ - $\tilde{\text{M}}^{2+}$	82.0	1.67	11.70	51.85	10 ⁷	10 ⁷
Cl ⁻ -wall	100.0	1.53	100	1000	1.5	1.0
M ⁺ -M ⁺	15.57	1.67	1.76	2.98	10 ⁷	10 ⁷
M ⁺ - $\tilde{\text{M}}^{2+}$	15.57	1.67	1.76	2.98	10 ⁷	10 ⁷
M ⁺ -wall	450.0	1.8	30	300	1.5	1.51
$\tilde{\text{M}}^{2+}\text{-}\tilde{\text{M}}^{2+}$	15.57	1.67	1.76	2.98	10 ⁷	10 ⁷
$\tilde{\text{M}}^{2+}\text{-wall}$	100	1.53	100	1000	1.5	1.0

¹J. W. Halley, A. Mazzolo, Y. Zhou, and D. Price, J. Electroanal. Chem. **450**, 273 (1998).

²S. Izvekov, A. Mazzolo, K. VanOpdorp, and G. A. Voth, J. Chem. Phys. **114**, 3248 (2001).

³E. Spohr, Electrochim. Acta **44**, 1697 (1999).

⁴W. Schmickler, Chem. Rev. (Washington, D.C.) **96**, 3177 (1996).

⁵A. Y. Lozovoi, A. Alavi, J. Kohanoff, and R. M. Lynden-Bell, J. Chem. Phys. **115**, 1661 (2001).

⁶E. Wernersson and R. Kjellander, J. Chem. Phys. **125**, 154702 (2006).

⁷Y. Ito, Electrochemistry (Tokyo, Jpn.) **73**, 545 (2005).

⁸G. B. Pan and W. Freyland, Chem. Phys. Lett. **427**, 96 (2006).

⁹D. M. Heyes and J. H. R. Clarke, J. Chem. Soc., Faraday Trans. 2 **77**, 1089 (1981).

¹⁰R. M. Esnouf and P. J. Grout, Philos. Mag. A **58**, 27 (1988).

¹¹O. J. Lanning and P. A. Madden, J. Phys. Chem. B **108**, 11069 (2004).

¹²M. J. Booth and A. D. J. Haymet, Mol. Phys. **99**, 1817 (2001).

¹³J. I. Siepmann and M. Sprik, J. Chem. Phys. **102**, 511 (1995).

¹⁴M. W. Finnis, R. Kaschner, C. Kruse, J. Furthmüller, and M. Scheffler, J. Phys.: Condens. Matter **7**, 2001 (1995).

¹⁵D. Marx and J. Hütter, *Ab Initio Molecular Dynamics: Theory and Implementation, Modern Methods and Algorithms of Quantum Chemistry*, NIC Series Vol. 1 (NIC, Jülich, 2000) (<http://www.fz-juelich.de/nic-series/> Volume1/); D. K. Remler and P. A. Madden, Mol. Phys. **70**, 921 (1990).

¹⁶S. de Leeuw and J. Perram, Mol. Phys. **37**, 1313 (1979).

¹⁷A. Szabo and N. Ostlund, *Modern Quantum Chemistry: Introduction to Advanced Electronic Structure Theory* (MacMillan, New York, 1982).

¹⁸M. Kawata and M. Mikami, Chem. Phys. Lett. **340**, 157 (2001).

¹⁹W. H. Press, B. P. Flannery, S. A. Teukolsky, and W. T. Vetterling, *Numerical Recipes* (CUP, Cambridge, 1992).

²⁰O. J. Lanning, Ph.D. thesis, University of Oxford, 2006.

²¹O. J. Lanning, S. Shellswell, and P. A. Madden, Mol. Phys. **102**, 839 (2004).

²²B. Morgan and P. A. Madden, J. Chem. Phys. **120**, 1402 (2004).

²³F. G. Fumi and M. P. Tosi, J. Phys. Chem. Solids **25**, 31 (1964); **25**, 45 (1964).

²⁴A. Kizza, Electrochim. Acta **51**, 2315 (2006).

²⁵C. H. Liu, K. E. Johnson, and H. A. Laitinen, *Molten Salt Chemistry* (Interscience, New York, 1964), pp. 681-733.

²⁶D. I. Leikis, K. V. Rybalka, E. S. Sevastyanov, and A. N. Frumkin, J. Electroanal. Chem. **46**, 161 (1973).

²⁷K. T. Tang and J. P. Toennies, J. Chem. Phys. **80**, 3726 (1984).